Liquid Crystal Elastomer with Integrated Soft Thermoelectrics for Shape Memory Actuation and Energy Harvesting

*Mason Zadan, Dinesh K. Patel, Andrew P. Sabelhaus, Jiahe Liao, Anthony Wertz, Lining Yao, and Carmel Majidi**

Liquid crystal elastomers (LCEs) have attracted tremendous interest as actuators for soft robotics due to their mechanical and shape memory properties. However, LCE actuators typically respond to thermal stimulation through active Joule heating and passive cooling, which make them difficult to control. In this work, LCEs are combined with soft, stretchable thermoelectrics to create transducers capable of electrically controlled actuation, active cooling, and thermal-to-electrical energy conversion. The thermoelectric layers are composed of semiconductors embedded within a 3D printed elastomer matrix and wired together with eutectic gallium–indium (EGaIn) liquid metal interconnects. This layer is covered on both sides with LCE, which alternately heats and cools to achieve cyclical bending actuation in response to voltage-controlled Peltier activation. Moreover, the thermoelectric layer can harvest energy from thermal gradients between the two LCE layers through the Seebeck effect, allowing for regenerative energy harvesting. As demonstrations, first, closed-loop control of the transducer is performed to rapidly track a changing actuator position. Second, a soft robotic walker that is capable of walking toward a heat source and harvesting energy is introduced. Lastly, phototropic-inspired autonomous deflection of the limbs toward a heat source is shown, demonstrating an additional method to increase energy recuperation efficiency for soft systems.

1. Introduction

Liquid crystal elastomers (LCEs) are a class of shape memory polymers composed of loosely crosslinked polymer networks that exhibit reversible shape change during transitions from nematic to isotropic phases.[1] They have become increasingly popular as actuators for use in soft robotics,[2–4] wearable computing and haptics,[5,6] and shape morphing matter[7–9] on account of their muscle-like work density and contraction strain[10–14] and ability to be printed or patterned into a wide range of geometries.[15,16] In most robotics and engineering applications, LCE-based actuators are stimulated thermally using an external heat source or electrically through Joule heating using an integrated wire or embedded network of percolating particles. Previous work has focused on heating LCEs primarily through Joule heating[6,12,13,17,18] with many of these applications using liquid metal[19–21] and wavy electronics[12,13,22,23] as a heating element. However, a key limitation of these approaches is their reliance on open-loop heating and passive cooling. This results in slow changes in temperature and a limited ability to control the speed and profile of the LCE actuator response. In particular, actuation speeds can be slow due to the LCE's low thermal conductivity of 0.3 W m^{-1} K^{-1}[20] and cooling speed is greatly limited due to heat transfer by convection rather than conduction. The latter results in cooling times that can take five times,[12,24] 10 times,[13] or even up to 50 times[25] the activation time in order for the LCE to cool under ambient conditions and return to its original state. Moreover, faster actuation speeds have been shown to require longer cooldown times due to the greater increase in temperature.[25] To decrease heating times, soft fillers such as liquid metal droplets have been embedded to increase the thermal conductivity of these architectures.[6] Issues with cooling times still persist, with these differences in heating and cooling times being functions of the difference in the rate of heat transfer between conduction (heating) and convection (cooling); smarter approaches are needed to address this issue.

There have been recent efforts to improve the speed and control of LCE actuators through novel methods of stimulation,[26] though most of these introduce significant mechanical

M. Zadan, A. P. Sabelhaus,[+] C. Majidi
Department of Mechanical Engineering
Carnegie Mellon University
Pittsburgh, PA 15213, USA
E-mail: cmajidi@andrew.cmu.edu
D. K. Patel, L. Yao
Human-Computer Interaction Institute
Carnegie Mellon University
Pittsburgh, PA 15213, USA
J. Liao, A. Wertz, C. Majidi
The Robotics Institute
Carnegie Mellon University
Pittsburgh, PA 15213, USA

[+]Present address: Department of Mechanical Engineering, Boston University, Boston, MA 02215, USA

design challenges for robotics. Compared to external convection heating and Joule activation, a faster and more controlled LCE response can be achieved by pumping hot and cold fluid through embedded microfluidic channels[26] or by utilizing compressed air.[25] However, this leads to the need for bulky heating units and liquid pumps for actuation. Other approaches for actuating LCEs have included electromagnetic (EM) radiation, including visible,[27–29] microwave,[30] and infrared light (IR).[31] However, these methods are unrealistic for robust autonomous robotic motion since the LCE must be in the range of directional EM emitters, which typically require a visual line of sight since the wavelengths in this range cannot penetrate opaque structures. Moreover, the emitted EM radiation does not usually enable the precision needed for controlled robotic actuation. Approaches with magnetic actuation have also been tried, but these require large external magnets and are susceptible to potential interference issues with the environment, such as metal around where the robot is navigating through.[32] While promising, these approaches are still limited in their ability to enable robust and repeatable heating and cooling for controllable actuation. They are also not compatible with lightweight mobile or wearable robotic devices.

A second challenge with LCE actuators is the low energy efficiencies associated with the existing methods of stimulation. Heating through Joule activation requires high input power (≈1–10 W) over long periods of time (≈10–100 s) to heat LCEs above their nematic-to-isotropic transition temperatures.[18,25,33] Moreover, during intracycle cooling, this energy is lost through convection cooling. Likewise, although convection heating and EM-based actuation methods can increase actuation speeds, they are also susceptible to inefficiency on account of indiscriminately directing energy over large volumes.[34] These prohibitive properties make it difficult for LCE-based actuators to become viable options when compared to other actuation modalities. Moreover, such challenges are not limited to LCEs and are also observed in other thermally activated shape memory materials such as nickel–titanium shape memory alloys (SMAs), which suffer from low energy efficiencies of 1–2%.[35] A possible solution to increase the efficiency is recycling some of the otherwise-wasted thermal energy back into the actuator or host device. One of the future potentials and advantages of soft robotic systems is the ability to recover energy that is momentarily stored within soft materials and actuators that would otherwise go unused.[36] In the case of LCEs, the ability to recover energy from residual heat and thermal gradients could contribute to improved energy efficiency and longevity of the host electronic device or robotic system.

In this paper, we simultaneously address both challenges by combining LCEs with a thin thermoelectric layer that is soft, stretchable, and conforms to LCE deformation. The thermoelectric device (TED) layer is composed of n-type and p-type bismuth telluride (Bi_2Te_3) microcubes that are wired together with eutectic gallium–indium (EGaIn) liquid metal interconnects and embedded within a 3D printed elastomer matrix (**Figure 1**a). This approach to create TEDs that are soft and elastic builds on recent research that has focused on combining Bi_2Te_3 with elastomers and liquid metals to create thermoelectric generators (TEGs) that are flexible and stretchable for wearable applications.[37–44] Previous work has also shown that soft TEDs with integrated wavy-electronic copper interconnects are viable candidates for thermohaptic feedback in virtual reality.[43,44] Here, we show that patterned liquid metal is similarly promising as interconnects within a soft TED architecture. Depending on the mode of operation, the soft TED functions as a Peltier heating/cooling device to control the contraction of the LCE layers or as an energy generator that uses the Seebeck effect to convert thermal gradients into electricity. In the Peltier mode, it can be used as thermal stimuli for LCEs, which exhibits the shape memory response presented in Figure 1b. This thermoelectric layer is then placed between two pre-strained pieces of LCE (Figure 1c). We term the final device an "LCE-TED." When current is applied across the leads of the soft
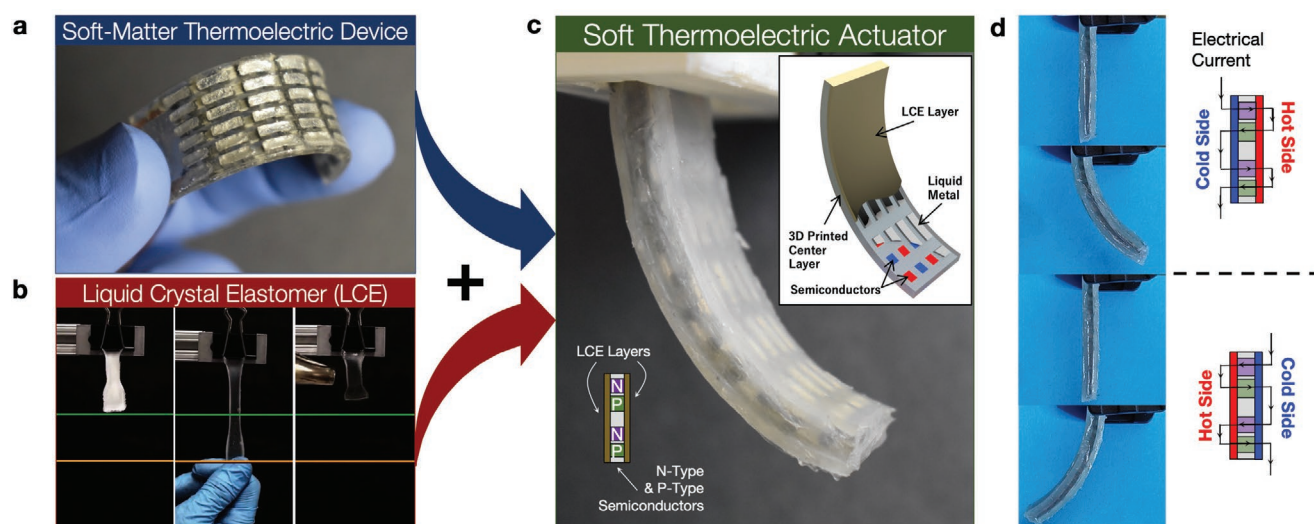

Figure 1. a) A stretchable 90 semiconductor soft-matter TED under deformation highlighting conformity of LM traces and 3D printed center layer. b) Images showing the responsiveness of the LCE shape memory polymer to heat. c) LCE-TED soft limb during actuation with right side heating and left side cooling. The inset represents a schematic diagram showing LM traces and semiconductors beneath the LCE layer. d) Images highlighting how the change in the current direction across semiconductors reverses the direction of actuation using only one input source.

**ADVANCED
SCIENCE NEWS**

www.advancedsciencenews.com

**ADVANCED
MATERIALS**

www.advmat.de

TED, the right side of the LCE-TED transducer contracts as the LCE heats from Peltier heating that induces uniform bending of the transducer in the counterclockwise (CCW) direction. Reversing the flow of current causes the right side that was previously heating to subsequently actively cool and the left side of the device to heat up, resulting in bending in the clockwise (CW) direction (Figure 1d). By incorporating a soft and stretchable TED, both high and low temperatures can be applied to the LCE layers at the same time with only one electrical input. By placing the TED in the center of the actuator, this ensures that heat is both being delivered effectively to the contracting side of the LCE as well as cooling the opposite side actively.

Through a series of soft robotics demonstrations, we demonstrate our design's potential to significantly improve the adoption of LCEs in practical applications. First, the closed-loop position control of our LCE-TED shows fast and accurate tracking due to active cooling. Prior applications of feedback in LCE-based robotic actuators are few and focus on sensing capabilities.[20,45] Most are only proof-of-concept, are relatively slow, and either lack full pose feedback for the robot[13] or are nonspecific about the feedback procedure.[25] In each case, the lack of cooling (i.e., a negative control input) limits the ability to apply traditional control analysis techniques. Other types of antagonistic thermoelectric actuators can be modeled with a bidirectional control input; however, these require either careful techniques to avoid overheating,[46] external cooling hardware,[47] or highly advanced constitutive models.[48] Our device's tracking control demonstration, using a theoretically-grounded feedback procedure, overcomes each of these drawbacks.

Second, a soft robot built from two of our actuators shows the LCE-TED locomoting to a heat source and harvesting energy while stationary. Although simple in design, this two-limbed walker demonstrates the potential for creating soft robotic systems that can harvest some of their electrical power from energy in the environment. Lastly, to further increase voltage harvesting potential, we highlight the "physical intelligence" of this transducer to autonomously orient itself closer to a heat source, which allows for more electricity to be generated through the Seebeck effect. This feature is loosely inspired by phototropism, in which a plant responds and moves toward a light source. Together, these demonstrations show significant promise for robots built from soft LCE-TED actuators.

2. Soft Thermoelectric Layer

We fabricate the TED layer with an array of n- and p-type Bi_2Te_3 semiconducting chips that are wired in series using EGaIn liquid metal traces. The chips are embedded inside an elastomer matrix that is 3D printed using a Digital Light Processing (DLP) method and sealed with a UV curable ink.[49] As shown later, this soft TED enables the operation of both the Peltier and Seebeck effect and is mechanically compatible with layers of LCE placed on the top and bottom surface. Figure S1 (Supporting Information) depicts steps for device fabrication. Further, details on 3D printing, fabrication parameters, and semiconductor properties can be found in the Experimental Section, and additional images of fabricated

devices are shown in Figure S2 (Supporting Information). The TEDs are made with a maximum of 90 semiconducting chips ($1.4 \times 1.4 \times 1.6$ mm) in six rows of 15 with overall active dimensions of $43.0 \times 14.5 \times 3.4$ mm and a surface area fill of 28%.

2.1. Seebeck Characterization

Experimental measurements for energy harvesting through the Seebeck effect are presented in **Figure 2**a,b. The voltage V generated by a temperature difference ΔT is estimated as $V = n\alpha\Delta T$, where n is the number of n-type/p-type semiconductor pairs and α is the Seebeck coefficient of the bismuth telluride.[50] Figure 2a shows the open-circuit voltage generated from changing temperature differentials across the TED. A linear relationship was found between temperature difference and voltage in line with the established relationship of $V = n\alpha\Delta T$. At $\Delta T = 30$ and 60 °C, voltages of 54.7 ± 2.0 mV and 107.1 ± 0.7 mV was recorded as an increase in temperature corresponds to larger charge buildup across junctions. While voltages are low, they are in the range needed for voltage boosting to power small microcontrollers (LTC3108 Analog Devices).

By impedance matching the internal resistance of the thermocouple arrays with an external resistor, power (P) can be optimized for the highest possible power output when the device is in contact with a heat source.[51] Figure 2b inset gives a diagram of the TEG and external resistor in parallel with a multimeter setup recording the voltage output. By recording voltage output (V_{TEG}) and varying the external resistance (R_{ext}) the power output is determined by

$$P = \frac{V_{TEG}^2}{R_{ext}} \tag{1}$$

Figure 2b gives external resistance vs power and power density for temperature differentials of $\Delta T = 30$–60 °C. Peak power was recorded at an external resistance of 1.5 Ω, which is in line with the recorded internal resistance at room temperature of ≈1.5 Ω, indicating that impedance matching is taking place as expected. At $\Delta T = 60$ °C, max. power of 1.61 mW and 236 μW cm^{-2} was recorded, which corresponds to a 32.7 mA current (Figure S3, Supporting Information). This is a ≈2.75 power density increase over previous work at the same temperature differential.[38]

When resistance is plotted against voltage (Figure S4, Supporting Information), an increase in external resistance corresponds to a sharp increase followed by leveling off of voltage when $R_{ext} ≈ 10$ Ω. Voltages begin to approach open-circuit voltage at these higher resistor values as the impedance increases. For instance, at $\Delta T = 60$ °C $V_{oc} = 107.1 \pm 0.7$ mV (Figure 2a) and with an external resistance of 67.9 Ω, a similar voltage of 104 mV was recorded (Figure S4, Supporting Information). This has been shown before as an increase in impedance from the external parallel resistor leads to a voltage output approaching an open-circuit voltage.[38] In this case, voltage saturates at an external resistance of around an order of magnitude above internal resistance.
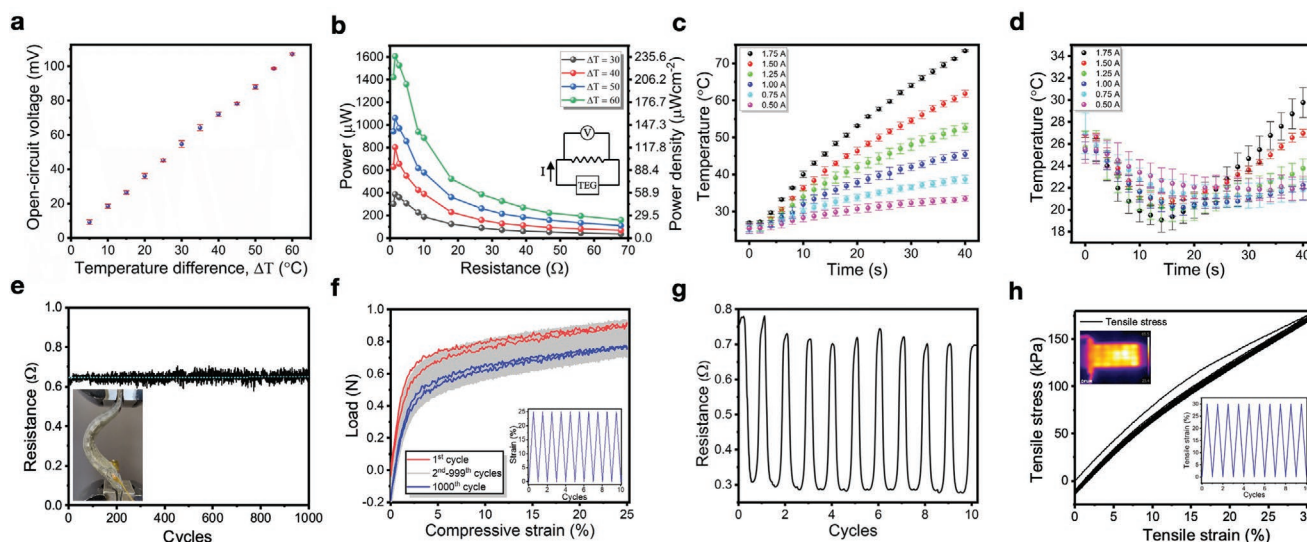
Figure 2. a) Temperature difference across a soft-matter TEG vs open-circuit voltage, confirming a linear relationship with a small error ($n = 3$). b) Resistance versus power and power density for varying temperature differentials. Inset: Circuit diagram for impedance matching. c) Time versus temperature for varying currents on the heating side of a 90 semiconductor TEG ($n = 3$). d) Time versus temperature for varying currents on the cooling side for a 90 semiconductor TEG ($n = 3$). e) Graph of change in resistance for 1000 cycles at 25% compression highlighting no mechanical or electrical failure. Inset: 44 semiconductor TEG at 25% compression in the universal load frame. f) Strain versus load for 10 000 compressive cycles. g) Change in resistance for 10 cycles at 30% axial strain in the universal load frame. h) Stress–strain curve for ten cycles at 30% axial strain showing no mechanical failure or damage. The thermal inset shows 44 semiconductor TEG heating properly after cyclic loading.

2.2. Peltier Characterization

Characterization of the Peltier effect for voltage-controlled heating/cooling is presented in Figure 2c,d. By applying a current across thermocouples in series, temperature differentials are created at the junctions as the thermocouple alternates from forward bias to reverse bias. This Peltier effect allows us to create the uniform and fast heating and cooling that is needed to give effective heat output and absorption to the LCE surrounding the actuators. To better understand these characteristics, the Peltier effect for LCE actuation was characterized by recording heating and cooling curves for the TEDs at varying currents. Increasing current increases the rate of temperature increase for heating curves as expected (Figure 2c). At 1.75 A, the TED generated 73.4 ± 0.3 °C at 40 s (Figure S5a, Supporting Information) with a power draw of 5.5 W, while at the lower current of 0.5 A at 40 s with a power draw of 0.4 W, the heat generated was 33.5 ± 0.8 °C with a leveling off of temperature increase in this time range.

While an increase in current corresponded to an increase in temperature, the relationship between cooling and current was much more complex. As there is no thermal management or heat sink used during these tests, heat tends to bleed across the 3D center layer. This is seen from the cooling data (1.75 A; Figure 2d) as the temperature drops quickly initially from an initial temperature of 25.6 ± 1.0 °C to 19.1 ± 1.1 °C at 14 s (Figure S5b, Supporting Information), followed by a sharp increase to 29.8 ± 1.4 °C at 40 s giving the maximum cooling effect of 6.5 °C. Having a local minimum followed by a sharp temperature increase is less prominent in lower currents where less heat is generated on the opposite ends of the semiconductors with less energy transferring as quickly across. At 0.5 A, the cooling side is 22.7 ± 1.2 °C at 14 s and 22.0 ± 1.1 °C at 40 s

with both values within the standard error of each other. This needs to be considered when actively cooling the TEGs as too high of a current will not necessarily lead to a lower temperature. Recent work by Jung et al. has identified underwater applications as a means to improve device performance.[52] Jung et al. showed that using water in contact with the TED as a heat sink led to an improvement in thermoelectric performance. To account for a wide range of operating environments and varying environmental temperature fluctuations, we conducted tests in a water environment. By operating the soft TED in water, we found no influence on heating behavior but did observe limited improvement in cooling performance (Figures S6 and S7, Supporting Information).

2.3. Mechanical Characterization

In order to confirm that the thermoelectric layer could perform effectively under the stresses of repeated use as actuators and energy harvesters without degrading electrically or mechanically, cyclical bending and axial strain tests were conducted. Figure 2e gives internal resistance data for 1000 cycles at 25% compression, with the dotted line representing the value of initial resistance. The data showed excellent stability for use in actuators during bending. An image of the device in the compressed state is given in the inset. After 1000 cycles, no mechanical or electrical failure was observed.

In addition, no significant increase in resistance was found after 1000 cycles indicating the 3D printed polymer center layer and LM traces are deforming without affecting contact resistance with the semiconductors during actuation. Under these loading conditions, plastic deformation occurs with changes in stress–strain curves between the first (red) and 1000th (blue)

**ADVANCED
SCIENCE NEWS**

www.advancedsciencenews.com

**ADVANCED
MATERIALS**

www.advmat.de

cycles (Figure 2f). It is also unclear why the load of the final cycle is higher than the lowest sets of cycles in the grayed-out region. Hysteresis was shown to occur intracycle as expected but in no way impacting actuator performance.

During operation in a soft actuator or robotic system, these TEDs will exhibit very little to no axial strain. Nonetheless, we demonstrate the ability of the soft TED to be cyclically loaded to 30% uniaxial strain for 10 cycles (Figure 2g). Resistance dropped from ≈0.7 Ω at 0% strain to ≈0.3 Ω at 30% strain. No damage or trends in resistance were detected during these tests. In addition, no mechanical or electrical failure occurred. This decrease in resistance could be caused by a decrease in contact resistance between semiconductors and LM traces from transverse compression during axial loading. This should not be an issue for the actuators as very little axial strain occurs during actuation. After the test was completed, the voltage was applied across the terminals of the device. The device functioned well with no semiconductors failing to generate heat (Figure 2h thermal inset). Mechanical stability was observed after the first cycle of axial loading, as seen in Figure 2h. There is limited hysteresis during loading for the other nine cycles showing mechanical stability of the 3D printed components under extreme conditions.

3. Thermoelectric-LCE Transducer

By placing photoinitiated pre-strained LCE onto each side of the TED, we can create a flexural actuator in which the opposing LCE layers are simultaneously heated and cooled. LCE fabrication was based on a process developed by Yakacki et al.[53] with additional information given in the Experimental Section. For fabricating actuators, the LCE was pre-strained to 80%, UV cured, and adhered to each side of the TED (Figure 1c; Figure S8, Supporting Information).

Actuator angle and force output were characterized to better highlight the actuator characteristics and inform controls and robotic applications given in the next section. Results indicated that these actuators have a high angle of stroke, can generate significant force for an actuator made of soft components, and repeatedly and controllably deliver that same force output as a function of time cyclically for a high number of repetitions. As opposed to Joule-heated actuators with one direction of motion per voltage input, these TED actuated soft muscles can operate in positive and negative angular domains above and below zero degrees bending angle using only one input.

3.1. Characterization of Actuator Bending

By reversing the input voltage from positive to negative, the actuator can both actively heat and cool the opposing surfaces at the same time, reversing the direction of actuation. A representative cycle is shown in Figure 1d, with time vs angle results shown in **Figure 3**a. With a positive voltage of 2.9 V applied followed by −2.9 V, max. angles of 27° and −27° are reported. The maximum angular velocity recorded during testing was 2.5° s^{-1} (Figure S9, Supporting Information). The ratio of time from 0° to 27° and 27° back to 0° is 1:0.43 for one cycle. This multidirectional actuation and active cooling is an order of magnitude faster compared to actuation cycles (1:10) of previous single input Joule-heated actuators that require ambient air cooling.[13] As there is a defined relationship between temperature and contraction,[53] these actuators operate better when running warm. This explains the steeper slope in actuation in the negative direction when the negative voltage is applied. The LCE has already warmed up due to some thermal bleeding from the heated side onto the cooling side, as seen in Figure 2d. This, along with stored elastic potential energy, accounts for the faster actuation upon voltage reversal. The first of the 99 blocking
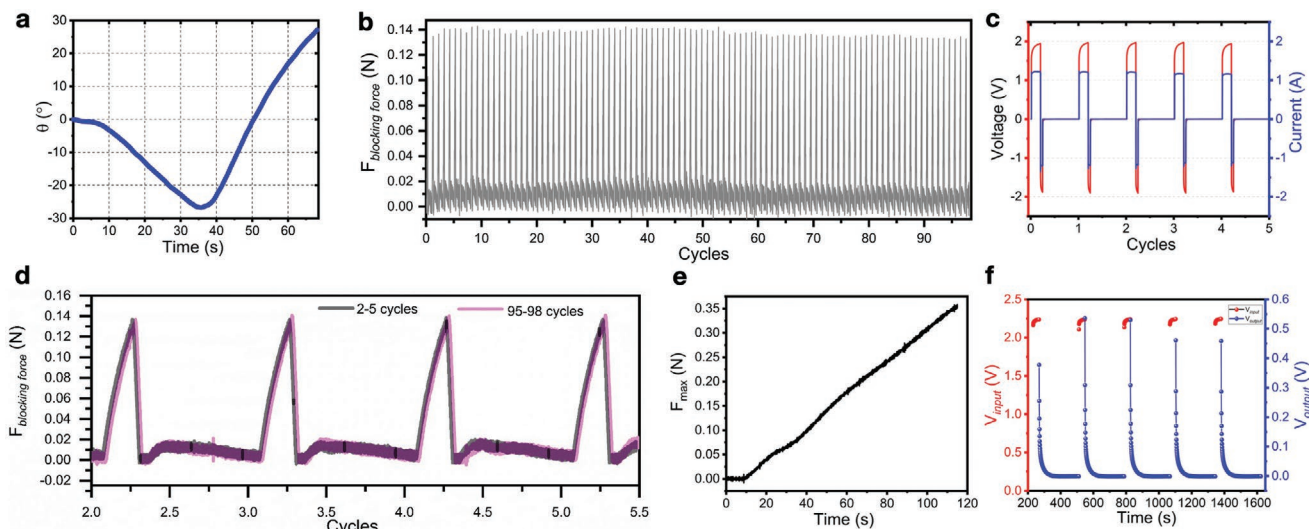

Figure 3. a) measurement of time versus stroke angle for a soft-matter actuator running at 2.9 V followed by −2.9 V. b) 99 cycle blocking force test at 1.7 V highlighting robustness and stability of actuator. c) Voltage and current values for five representative cycles for the blocking force test. d) Comparison of cycles 2–5 and 95–98 highlighting high stability and no mechanical or electrical damage during a high cycle load. e) Max. blocking force test of time versus force at 2.9 V to determine a max. force at break of 0.35 N. f) comparison of voltage inputted during actuation through the Peltier effect (red) and voltage outputted through the Seebeck effect during cooldown cycles (blue), highlighting regenerative energy recycling.

**ADVANCED
SCIENCE NEWS**

www.advancedsciencenews.com

**ADVANCED
MATERIALS**

www.advmat.de

force cycles in Figure 3b also highlights this characteristic as the initial cycle is the only force output that varies significantly from the others and represents a warmup cycle.

3.2. Force Output

Figure 3b shows a plot of time vs force output for the LCE actuator blocking force test for 99 cycles. Using an H-bridge circuit, the device was actuated for 95 s at 1.7 V into the load cell, 22 s at −1.7 V in reverse until a 0° angle, and 380 s of cooling time at 0 V for 99 cycles. Figure 3c graphs time vs voltage and current for five representative cycles. While power source voltage is constant along with current, the voltage across the actuator varies from 1.5–2.0 to −1.5 to −2.0 V to 0 V per cycle as varying semiconductor resistances inside the device and across the pins of the H-bridge metal–oxide–semiconductor field-effect transistors (MOSFETs) (used to reverse current directions) affect voltage. With an average max. force output of 0.138 N and a small standard error of 0.003 N for 98 cycles, high repeatability, stability, and robustness are shown.

To highlight force output stability and consistency, cycles 2–5 are compared to cycles 95–98 in Figure 3d. These force output curves are almost identical with max. output along with heating and cooling slopes being indistinguishable between initial and final cycles. Intracycle, the importance of running these actuators "warm" for faster actuation is again shown as only 23% of the positive actuation time is required to return to zero bending angle. By running this actuator at a higher voltage of 3.2 V, we obtained a max. force output of 0.35 N at break confirming high force output for a soft robotic muscle. By using thin LCE materials as well as low aspect ratio semiconductors, we were able to keep the second bending moment low in order to decrease flexural rigidity stiffness and achieve large bending curvatures. Compared to the commercially available 1.37 mm-diameter coiled nitinol shape memory alloy wire (Flexinol, Dynalloy inc), the force outputs are comparable with a heating and cooling force output of 0.39 N and 0.17 N for Flexinol, respectively. By defining a figure of merit (FoM) for this device as $U_e/(U_e + U_t)$ where U_e is the elastic energy and U_t is the thermal energy,[54] we determine an FoM of 0.0008 for one cycle at 3.2 V. Further information is given in the "Transducer Efficiency" section of the Supporting Information along with Figure S10 (Supporting Information). Although low, this FoM is in line with other thermally driven soft actuators and can potentially be increased by altering the dimensions of the device layers.[54]

3.3. Regenerative Energy Harvesting

In between actuation cycles, a portion of the heat applied to the system during Peltier heating can be converted back into voltage through the Seebeck effect. Much like electric car regenerative energy harvesting from induction motors during braking, in which induction motors double as energy harvesters when torque is applied to the motor, the LCE-TED actuators have similar characteristics through electrothermal instead of kinetic energy conversion. We introduce regenerative energy harvesting into a soft actuator as a proof of concept. We tested this unique characteristic for five cycles, inputting heat into the system through Peltier heating for 35 s at 2.2 V, followed by recording the voltage output during a 4 min cooldown as the actuator moved back to the rest position. Results are shown in Figure 3f, with the left y-axis showing voltage input and the right y-axis showing generated voltage. The maximum generated voltage of 0.53 V was recorded. Voltage drops quickly, and heat transfers across the system as it approaches a steady state. By analyzing one cycle at 2.7 V across the transducer for 50 s and 0 V for 6 min of energy harvesting (Figure S11, Supporting Information), we can determine the efficiency of applied vs generated energy to be $\eta = 0.03\%$. For more details, see the "Regenerative Energy Harvesting Efficiency" section in the Supporting Information. While this efficiency is not high enough to increase the range of the actuator in a meaningful way, we introduce this as a proof of concept and hope it spurs further investigation of efficient energy recovery methods that can be used for soft actuators. Potential methods to improve efficiency include decreasing the thermal resistance between the semiconductors and LCE layer to guarantee better contact before the temperature differential across the entire device degrades due to heat conduction. This unique feature introduces a new approach for more energy-efficient soft robotic actuators.

4. Demonstrations

4.1. Position-Controlled Actuation Demonstration

A position-control feedback test was performed to track deflections of the soft LCE-TED actuator, here considered to be a single-degree-of-freedom robot limb. Using the feedback procedure discussed in the Experimental Section, the limb held alternating angles of + 5° or −5° for 50 s each (**Figure 4**a). This response was verified using two different soft limb prototypes that were tested with the same control system. Results show that the actuator can quickly switch between positive and negative angles (Figure 4b), as anticipated from the characterization tests. Even though the control system never applies the full 100% duty cycle power (see Supporting Information for more discussion), the limb still reaches its desired angle after only ≈20 s. This would not be possible with passive cooling alone. The position error reaches <0.5° after settling, which is more than sufficient for most soft robotics applications.[46]

4.2. Soft Walker Demonstration

To demonstrate the use of these transducers in a robotic system, we have developed an LCE-TED walker capable of walking toward a heat source and harvesting energy. The walker is composed of two LCE-TED limbs that are oriented 90° apart and connected at the ends. At the distal end where the limb makes contact with the ground, an angled and jagged copper shim is adhered in order to enable anisotropic friction[12,55] and allow the walker to move in a forward direction. By reversing the voltage direction during actuation, we induced forward movement as the limbs contracted and expanded, first pulling together and then pushing apart. Additional gait information is
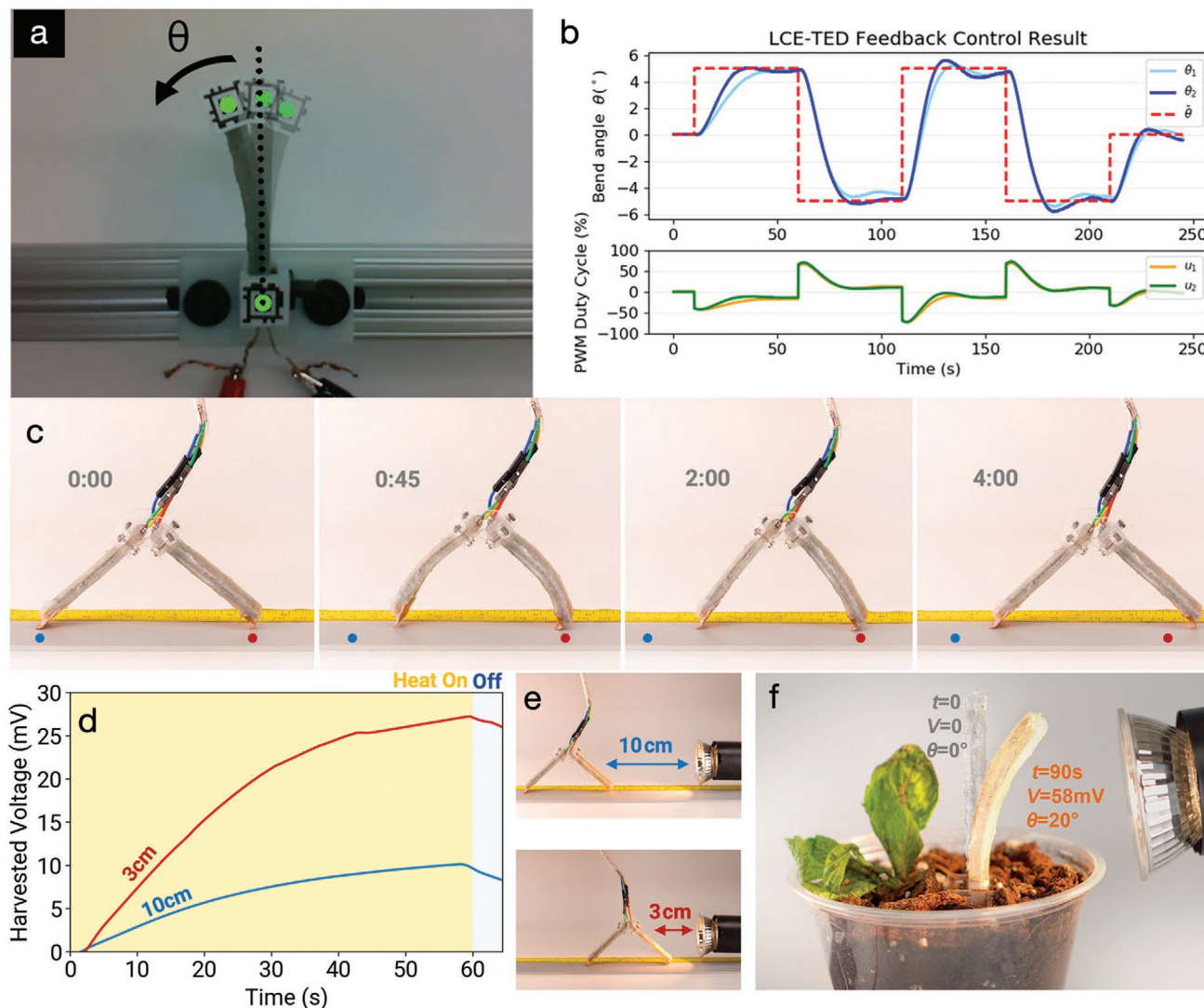
**ADVANCED
SCIENCE NEWS**

www.advancedsciencenews.com

**ADVANCED
MATERIALS**

www.advmat.de

Figure 4. a,b) Position control test of LCE-TED actuator prototypes. a) The target robot limb pose is specified as a deflection angle, measured using a computer vision system. b) Feedback control demonstrates low-error tracking of deflection angle, verified on two different actuator prototypes (1 and 2). c–e) Walker demonstration of LCE-TED actuators. c) Gait mechanics for one gait cycle of the two-legged soft walker. Specific actuation times are given in the Experimental Section. d) Graph of energy harvesting from the front limb at the initial and final positions of the soft walker, highlighting the walker's ability to move over to a power source and passively generate voltage during hibernation. e) Images of initial vs final position away from the energy source corresponding to (d). f) Image of an LCE limb exhibiting physical intelligence as it tracks toward a heat source and increases the harvested voltage.

given in the Experimental Section. Figure 4c presents images of a representative gait cycle.

The task planned for this robot was to move itself over to an energy source, in this case, a heat lamp, and generate continuous electricity. Distance between the limb and energy source is key to overcoming the heat loss of air's low thermal conductivity. Initially, we recorded the voltage output of the front limb at a distance of 10 cm away from the heat source. The walker then actuated over to the heat source in order to record a higher voltage output (Figure S12 and Video S1, Supporting Information). After re-recording the voltage, we found a much higher voltage output when the limb is closer at 3 cm to the heat lamp (Figure 4d,e; Video S2, Supporting Information). When reaching the heat source, the soft walker enters a "hibernation"

state; during that time, it can generate power indefinitely from a heat source. We also found that as the limb generated voltage, the limb closest to the heat lamp begins to heat up and actuates in response to the ambient heating. This limb bending causes the walker to pull even closer to the heat lamp (Video S2, Supporting Information).

4.3. Phototropism-Inspired Energy-Harvesting Demonstration

For the soft walker demonstration, we observed that the limb closest to the heat source would bend in response to the ambient heating and pull the walker closer to the heat lamp. From this, we infer a passive "physical intelligence" of the

transducer by which it will autonomously move toward the energy source.[56] This effect, which loosely resembles phototropism and heliotracking SMPs,[57,58] is further examined with the demonstration presented in Figure 4f. By placing a soft limb vertically near a heat source and applying no voltage to the limb, we see the soft transducer autonomously sense and bend toward the heat source (Figure S13, Supporting Information). Bending decreases the distance between the thermoelectric layer and the heat source, which can cause an increase in the amount of electricity that is generated (Figure S14, Supporting Information). When the heat source is turned off, the voltage and angle decrease as the limb moves away from the heat source and returns to its naturally straight configuration (Video S3, Supporting Information). Comparison tests were conducted with and without the LCE layer in which the heat source is placed adjacent to the base of the actuator and oriented so that heat is directed upwards (parallel to the actuator). These measurements show an improvement in voltage output when LCE is incorporated into the limb. This is because LCE actuation will cause the limb to autonomously bend toward the heat source and experience a larger surface area over the heat source leading to a larger temperature differential. Unlike the LCE-integrated limb, the passive limb does not bend and exhibits a voltage output plateau of 10 mV after 50 s of exposure to the heat source. In contrast, the autonomously responsive limb with LCE exhibited a greater than 2× voltage output with a maximum voltage output of 22 mV (Figure S14, Supporting Information). This energy-harvesting demonstration shows the physical intelligence of the LCE-thermoelectric transducer and suggests the potential for future soft robotic systems to generate energy from their surroundings in between actuation cycles or during periods of hibernation (e.g., sleep mode) or low-power operations.

5. Conclusions

This work has demonstrated the use of a deformable, 3D printed TED in LCE actuators to enable both active heating and cooling of LCEs along with energy harvesting. By controlling heating and cooling actively, multidirectional actuation can be controlled with one input improving actuation times over ambient cooling by an order of magnitude. With both heating and cooling, we have shown a practical feedback control example, with a rapid bidirectional response and no external cooling hardware, suitable for integration into soft robots.

Additionally, this work has introduced the concept of soft actuators with intrinsic energy-harvesting capabilities for environmental energy harvesting along with regenerative thermal recycling. The latter allows for the recycling of otherwise wasted thermal energy and is analogous to regenerative braking used in induction motors for electric vehicles. By exploiting temperature gradients in nature or by exploiting internal temperature differentials between the LCE layers, the Seebeck effect converts thermal energy into electricity that can be used for subsequent actuation cycles. We highlight the potential of LCE-TED actuators in a tethered two-legged-walker demonstration in which the walker moves to a heat source to generate voltage. Lastly, these limbs demonstrate a form of physical intelligence in their ability to autonomously reconfigure themselves to increase the amount of energy harvested from an external heat source.

Future areas of improvement and current limitations center around thermal management. These actuators still require a prolonged cooldown time in between cycles that can take over 3× the actuation time at low voltages (Figure 3b) and up to 6.5× when larger activation voltages are used. Each LCE sheet of the LCE-TED limb is not independent of the other, with heat transferring across the 3D printed elastomer separation layer during prolonged actuation. This can lead to heat saturation within the actuator due to poor heat transfer through convection cooling and can produce high stresses at both interfaces, leading to delamination from the TED layer. One solution is increasing the bonding strength without increasing structural rigidity through stronger adhesives. Separately, decreasing thermal conductivity between the LCE sheets by taking full advantage of 3D printing for creating thermally insulating metamaterials may be another promising direction.

While these approaches would allow the LCE-TED-based limbs to operate for longer cycles, they do not address the intercycle cooldown time limitations. For this, the focus must be shifted to a new generation of high thermal conductivity deformable heat sinks to aid in convective cooling. Liquid metal embedded elastomer (LMEE) composites have been shown to have high mechanical compliance along with high thermal conductivities.[59] Previous work has shown LMEE composite's potential in TED-based systems for thermal management.[60,61] Further efforts to incorporate such material architectures and manufacturing methods could lead to additional improvements in LCE-TED performance. Lastly, we see the potential for future work in the integration of these transducers into a soft robot to realize the potential of LCE-TED limbs more fully. Untethered soft robotic platforms such as those explored by Patterson et al.[62] are a potential candidate to more fully develop the energy harvesting and controls potential introduced here.

6. Experimental Section

Elastomeric Resin Composition: The elastomeric resin used for 3D printing the center layer and sealing the LM traces comprises 49.02 wt% of epoxy aliphatic acrylate (EAA, Ebecryl 113, Allnex USA), 49.02% of aliphatic urethane acrylate (AUD, Ebecryl 8413, Allnex, USA) and 1.96% TPO (diphenyl(2,4,6-trimethylbenzoyl)phosphine oxide, Genocure TPO, RAHN USA Corp.) as the photoinitiator. TPO was dissolved in elastomeric monomers in a hot water bath at 86 °C.

3D Printing: 3D printing was performed using a DLP-based 3D printer (PicoHD@27, Asiga). This printer was operated by a top-down DLP system with a digital mirror device (DMD) and a UV–LED light source operating at 385 nm. The printer was maintained at 40 °C during printing, and each layer was irradiated for 0.5 s, and layer thickness was 100 µm. The detailed printing parameters are included in Table S1 (Supporting Information). The printed structures were sonicated with isopropyl alcohol (IPA) for 3 min to remove the uncured resin.

Thermoelectric Device Fabrication: The center layer (53 × 14 × 1.6 mm), which acted as a substrate for the LM channels and semiconductors, was printed using a DLP 3D printer (Figure S1-i, Supporting Information). This 3D printing process was based on previous work by Patel et al.[49] The center layer consisted of 1 mm wide and 0.4 mm deep channels for LM interconnects and holes for semiconductors (Figure S1-ii, Supporting Information). Depending on the desired configuration 44–90 1.4 × 1.4 × 1.6 mm 99.99% purity Bi_2Te_3 semiconductors (Wuhan

Xinrong New Materials Co., Ltd.) were placed into $1 \times 1 \times 1.6$ mm holes. This was followed by a post-curing in a UV chamber (CL-1000 Ultraviolet Crosslinker, UVP) for 3 min on each side to ensure a tight seal between substrate and semiconductors, mitigating LM shorting (Figure S1-iii, Supporting Information). A Stencil (polyester plastic McMaster-Carr) was then placed on the substrate, and EGaIn was airbrushed (Master G22) into the channels for 30 s (Figure S1-iv,v, Supporting Information). The device is then placed in a freezer at −30 °C solidifying the EGaIn traces below their melting temperature of 15.5 °C. The same UV curable ink used for the center layer was brushed onto the exposed LM traces using a paintbrush, covering them in a thin layer, and UV cured for 12 min at $\lambda = 365$ nm (Warson R838) (Figure S1-vi). This process was repeated on the backside with thin copper tape leads being attached before airbrushing (Figure S1-vii). The TED dimensions of the active part were $43.0 \times 14.5 \times 3.4$ mm with a 28% fill factor by surface area. More images of completed devices are available in Figure S2 (Supporting Information). Devices with 90 semiconductors were chosen for Peltier and Seebeck testing as this was the highest density of semiconductors that could be integrated without electrical shorting using our fabrication process. Increasing the semiconductor density increased energy-harvesting performance. Versions with 60 semiconductors that were evenly spaced were selected for transducer testing as they balanced heating uniformity and performance with flexural rigidity. Commercially available semiconductor pellets with dimensions of $1.4 \times 1.4 \times 1.6$ mm were chosen because of their low aspect ratio, which reduced the mechanical impedance to actuator bending and allowed for a relatively low electrical resistance.[63] However, we do note that the low aspect ratio would result in less ability to maintain a temperature differential due to the flow of heat through the thickness of the device.[63] The overall footprint of 53×14.5 mm was selected for the center layer since this was the maximum build area that can be achieved with the DLP 3D printer that was used. We used this high length-to-width ratio in order for direct implementation into soft robotic limbs.

LCE Fabrication: LCE fabrication was based on work by Yakacki et al.[53] RM257 monomer (1,4-bis-[4-(3-acryloyloxypropyloxy) benzoyloxy]-2-methylbenzene) (10.957 g; Wilshire Technologies; 95%) was dissolved into 3.40 g toluene (Sigma–Aldrich) at 80 °C for 20 min. Once cooled for 5 min 3.076 g EDDET (2,2′-(ethylenedioxy) diethanethiol) (Sigma–Aldrich), 0.488 g PETMP (pentaerythritol tetrakis (3-mercaptopropionate)) (Sigma–Aldrich), 0.077 g HHMP ((2-hydroxyethoxy)-2-methylpropiophenone) (Sigma–Aldrich), and 0.038 g DPA (dipropylamine) (Sigma–Aldrich) were mixed into the monomer solution and vortexed mixed for 1 min.[21] The mixture was then degassed for 1 min and poured into $11 \times 2 \times 0.2$ cm molds, with each mold creating enough LCE for one actuator. Samples oligomerize for 12 h at room temperature in a fume hood followed by 12 h in a vacuum oven (Across International) at 80 °C and 508 mm of Hg to evaporate the toluene. The LCE was uniaxially strained to 80%, and UV light (UVP, UVL-56 handheld UV lamp) was applied to crosslink for 30 min at 365 nm and 6 W, programming in a reversible prestrain of 39–45%. When pre-strained, the LCE strips were 1.1 mm thick and a 400 µm thick layer of Sil-poxy (Smooth-On) was then used to adhere the strips to each side of the TEG.

Thermoelectric Testing: Open-circuit voltage data were collected for three cycles at room temperature with the TEG placed on a hot plate with a 200g mass ensuring even contact. Thermoelectric testing was conducted without the LCE layer to better understand the TEDs themselves. Peak voltage was recorded as temperature differentials can decrease quickly. Power data were recorded by measuring voltage in parallel to the external resistor from the circuit given in the inset of Figure 2b. The TEG was placed on a hot plate with a 200 g mass ensuring even contact. Max. voltage in parallel was recorded for various resistor values. In between cycles, the TEG was cooled to ambient temperatures. For Peltier cycles, data were recorded for three passes for 40 s with a 90-semiconductor device being used. Temperatures were recorded using a thermal camera (FLIR C2) along with all tests being conducted at room temperature. The device was cool in between cycles.

Mechanical and Blocking Force Testing: All force and cyclical loading tests were conducted in a universal load frame (Instron 5969). Mechanical tests were run on a 44 semiconductor TEG modified to accept clamps for the universal load frame. Blocking force tests were performed on a 60 semiconductor actuator with a 10 N load cell placed right above, with the actuator placed parallel to the ground. The LCE-TED actuated into the load cell, determining force output. An Arduino microcontroller and power source along with an H-bridge of power MOSFETs were used to switch current directions for the blocking force test.

Feedback Control Test: The feedback control test used a hardware platform adapted from Patterson et al.[62] and Wertz et al.[46] The LCE-TED was clamped to a rigid frame, connected to an electronic circuit in an H-bridge configuration of power MOSFET transistors, and received positive or negative voltage via two pulse-width-modulation (PWM) signals. The nominal applied voltage across the device was calibrated to 2.9 V at the start of each test. A microcontroller changed the applied power by setting the positive/negative PWM duty cycle at time k, i.e., $u(k) \in [-1, 1]$, mapping negative duty cycles to the PWM connected to the "reverse" signal of the H-bridge. Two computer vision markers were placed on the test setup, one on the clamp and one at the tip of the actuator, so that a camera (Intel, Real Sense) measured the deflection angle of the soft limb ($\theta(k)$) in real time. Our control system takes a desired angle ($\bar{\theta}(k)$) and uses proportional-integral (PI) feedback to specify the PWM duty cycle as a function of the position error $e = \theta - \bar{\theta}$, i.e., $u(k) = K_p e(k) + \sum_{t=0}^{k} K_i e(t) \Delta t$. The controller gains K_p and K_i were estimated using various PI tuning rules from the literature. See Supporting Information for more specifics on electronics and control.

Robot Design: The soft robotic walker was designed with two 60-semiconductor LCE-TED actuators with their ends mounted 90 degrees apart in a laser-cut acrylic frame. 150 µm-thick, jagged copper feet were adhered using Sil-poxy onto the ends of the walker for directional dependent friction. In its rest state, the device is 65 mm high and 92 mm wide. Each limb was actuated with a 3.0 V power source. The actuation times were left limb +3 V, right limb −3 V for 45 s, then left limb 0 V, Right limb +3 V for 10 s, followed by a cool-down period of ≈6:30.

Statistical Analysis: The data were not preprocessed, outliers were not removed, and a smoothing algorithm was not used. For data with multiple trials, data were either represented individually for each trial or by a mean with a standard deviation shown. The data for Figure 2a,c,d and Figure S6 (Supporting Information) were for three trials tested on one device with mean and standard deviation shown. All resistance, current, and voltage measurements were recorded using an Agilent-34401A multimeter.

Supporting Information

Supporting Information is available from the Wiley Online Library or from the author.

Acknowledgements

**ADVANCED
SCIENCE NEWS**

www.advancedsciencenews.com

**ADVANCED
MATERIALS**

www.advmat.de

Conflict of Interest

The authors declare no conflict of interest.

Data Availability Statement

Research data are not shared.

Keywords

[1] S. W. Ula, N. A. Traugutt, R. H. Volpe, R. R. Patel, K. Yu, C. M. Yakacki, *Liq. Cryst. Rev.* **2018**, *6*, 78.

[2] X. Qian, Q. Chen, Y. Yang, Y. Xu, Z. Li, Z. Wang, Y. Wu, Y. Wei, Y. Ji, *Adv. Mater.* **2018**, *30*, 1801103.

[3] A. Kotikian, R. L. Truby, J. W. Boley, T. J. White, J. A. Lewis, *Adv. Mater.* **2018**, *30*, 1706164.

[4] Y. Wang, Z. Wang, Q. He, P. Iyer, S. Cai, Y. Wang, Z. Wang, Q. He, P. Iyer, S. Cai, *Adv. Intell. Syst.* **2020**, *2*, 1900177.

[5] N. Torras, K. E. Zinoviev, J. Esteve, A. Sánchez-Ferrer, *J. Mater. Chem. C* **2013**, *1*, 5183.

[6] M. J. Ford, C. P. Ambulo, T. A. Kent, E. J. Markvicka, C. Pan, J. Malen, T. H. Ware, C. Majidi, *Proc. Natl. Acad. Sci. USA* **2019**, *116*, 21438.

[7] A. Kotikian, C. McMahan, E. C. Davidson, J. M. Muhammad, R. D. Weeks, C. Daraio, J. A. Lewis, *Sci. Rob.* **2019**, *4*, eaax7044.

[8] Z. Shen, F. Chen, X. Zhu, K. T. Yong, G. Gu, *J. Mater. Chem. B* **2020**, *8*, 8972.

[9] C. P. Ambulo, J. J. Burroughs, J. M. Boothby, H. Kim, M. R. Shankar, T. H. Ware, *ACS Appl. Mater. Interfaces* **2017**, *9*, 37332.

[10] S. I. Rich, R. J. Wood, C. Majidi, *Nat. Electron* **2018**, *1*, 102.

[11] D. J. Roach, C. Yuan, X. Kuang, V. C. F. Li, P. Blake, M. L. Romero, I. Hammel, K. Yu, H. J. Qi, *ACS Appl. Mater. Interfaces* **2019**, *11*, 19514.

[12] J. M. Boothby, J. C. Gagnon, E. McDowell, T. Van Volkenburg, L. Currano, Z. Xia, *Soft Robot.* **2022**, *9*, 154.

[13] Q. He, Z. Wang, Y. Wang, A. Minori, M. T. Tolley, S. Cai, *Sci. Adv.* **2019**, *5*, eaax5746.

[14] S. Li, H. Bai, Z. Liu, X. Zhang, C. Huang, L. W. Wiesner, M. Silberstein, R. F. Shepherd, *Sci. Adv.* **2021**, *7*, eabg3677.

[15] T. H. Ware, M. E. McConney, J. J. Wie, V. P. Tondiglia, T. J. White, *Science* **2015**, *347*, 982.

[16] C. Zhang, X. Lu, G. Fei, Z. Wang, H. Xia, Y. Zhao, *ACS Appl. Mater. Interfaces* **2019**, *11*, 44774.

[17] T. A. Kent, M. J. Ford, E. J. Markvicka, C. Majidi, *Multifunct. Mater.* **2020**, *3*, 025003.

[18] C. Yuan, D. J. Roach, C. K. Dunn, Q. Mu, X. Kuang, C. M. Yakacki, T. J. Wang, K. Yu, H. J. Qi, *Soft Matter* **2017**, *13*, 5558.

[19] M. J. Ford, M. Palaniswamy, C. P. Ambulo, T. H. Ware, C. Majidi, *Soft Matter* **2020**, *16*, 5878.

[20] A. Kotikian, J. M. Morales, A. Lu, J. Mueller, Z. S. Davidson, J. W. Boley, J. A. Lewis, *Adv. Mater.* **2021**, *33*, 2101814.

[21] C. P. Ambulo, M. J. Ford, K. Searles, C. Majidi, T. H. Ware, *ACS Appl. Mater. Interfaces* **2021**, *13*, 12805.

[22] A. F. Minori, Q. He, P. E. Glick, I. Adibnazari, A. Stopol, S. Cai, M. T. Tolley, *Smart Mater. Struct.* **2020**, *29*, 105003.

[23] C. Wang, K. Sim, J. Chen, H. Kim, Z. Rao, Y. Li, W. Chen, J. Song, R. Verduzco, C. Yu, *Adv. Mater.* **2018**, *30*, 1706695.

[24] H. Liu, H. Tian, J. Shao, Z. Wang, X. Li, C. Wang, X. Chen, *ACS Appl. Mater. Interfaces* **2020**, *12*, 56338.

[25] H. Lu, Z. Zou, X. Wu, C. Shi, Y. Liu, J. Xiao, *Micromachines* **2021**, *12*, 736.

[26] Q. He, Z. Wang, Y. Wang, Z. Song, S. Cai, *ACS Appl. Mater. Interfaces* **2020**, *12*, 35464.

[27] H. Zeng, O. M. Wani, P. Wasylczyk, R. Kaczmarek, A. Priimagi, *Adv. Mater.* **2017**, *29*, 1701814.

[28] Z. Wang, K. Li, Q. He, S. Cai, *Adv. Mater.* **2019**, *31*, 1806849.

[29] M. Rogóż, K. Dradrach, C. Xuan, P. Wasylczyk, *Macromol. Rapid Commun.* **2019**, *40*, 1900279.

[30] X. Wang, Y. Wang, X. Wang, H. Niu, B. Ridi, J. Shu, X. Fang, C. Li, B. Wang, Y. Gao, L. Sun, M. Cao, *Soft Matter* **2020**, *16*, 7332.

[31] J. Liu, Y. Gao, H. Wang, R. Poling-Skutvik, C. O. Osuji, S. Yang, *Adv. Intell. Syst.* **2020**, *2*, 1900163

[32] S. Schuhladen, F. Preller, R. Rix, S. Petsch, R. Zentel, H. Zappe, *Adv. Mater.* **2014**, *26*, 7247.

[33] M. Wang, Z. W. Cheng, B. Zuo, X. M. Chen, S. Huang, H. Yang, *ACS Macro Lett.* **2020**, *9*, 860.

[34] Q. He, Z. Wang, Y. Wang, Z. Wang, C. Li, R. Annapooranan, J. Zeng, R. Chen, S. Cai, *Sci. Robot.* **2021**, *6*, abg2171.

[35] J. E. Huber, N. A. Fleck, M. F. Ashby, *Proc. R. Soc. London, Ser. A* **1997**, *453*, 2185.

[36] G. M. Whitesides, *Angew. Chem., Int. Ed.* **2018**, *57*, 4258.

[37] C. S. Kim, H. M. Yang, J. Lee, G. S. Lee, H. Choi, Y. J. Kim, S. H. Lim, S. H. Cho, B. J. Cho, *ACS Energy Lett.* **2018**, *3*, 501.

[38] M. Zadan, M. H. Malakooti, C. Majidi, *ACS Appl. Mater. Interfaces* **2020**, *12*, 17921.

[39] M. Zadan, C. Chiew, C. Majidi, M. H. Malakooti, *Multifunct. Mater.* **2021**, *4*, 012001.

[40] S. J. Kim, H. E. Lee, H. Choi, Y. Kim, J. H. We, J. S. Shin, K. J. Lee, B. J. Cho, *ACS Nano* **2016**, *10*, 10851.

[41] F. Suarez, D. P. Parekh, C. Ladd, D. Vashaee, M. D. Dickey, M. C. Öztürk, *Appl. Energy* **2017**, *202*, 736.

[42] S. H. Jeong, F. J. Cruz, S. Chen, L. Gravier, J. Liu, Z. Wu, K. Hjort, S. L. Zhang, Z. Bin Zhang, *ACS Appl. Mater. Interfaces* **2017**, *9*, 15791.

[43] J. Lee, H. Sul, W. Lee, K. R. Pyun, I. Ha, D. Kim, H. Park, H. Eom, Y. Yoon, J. Jung, D. Lee, S. H. Ko, *Adv. Funct. Mater.* **2020**, *30*, 1909171.

[44] J. Lee, D. Kim, H. Sul, S. H. Ko, *Adv. Funct. Mater.* **2021**, *31*, 2007376.

[45] S. Petsch, R. Rix, B. Khatri, S. Schuhladen, P. Müller, R. Zentel, H. Zappe, *Sens. Actuators, A* **2015**, *231*, 44.

[46] A. Wertz, A. P. Sabelhaus, C. Majidi, arXiv: 2110.09474, **2021**.

[47] A. Ianagui, E. A. Tannuri, *Mechatronics* **2015**, *30*, 126.

[48] M. Moallem, V. A. Tabrizi, *IEEE Trans. Control Syst. Technol.* **2009**, *17*, 184.

[49] D. K. Patel, A. H. Sakhaei, M. Layani, B. Zhang, Q. Ge, S. Magdassi, *Adv. Mater.* **2017**, *29*, 1606000.

[50] M.-Y. Lee, J.-H. Seo, H.-S. Lee, K. S. Garud, *Symmetry* **2020**, *12*, 786.

[51] S. Carreon-Bautista, A. Eladawy, A. Nader Mohieldin, E. Sanchez-Sinencio, *IEEE Trans. Ind. Electron.* **2014**, *61*, 5345.

[52] Y. Jung, J. Choi, Y. Yoon, H. Park, J. Lee, S. H. Ko, *Nano Energy* **2022**, *95*, 107002.

[53] C. M. Yakacki, M. Saed, D. P. Nair, T. Gong, S. M. Reed, C. N. Bowman, *RSC Adv.* **2015**, *5*, 18997.

**ADVANCED
SCIENCE NEWS**

www.advancedsciencenews.com

**ADVANCED
MATERIALS**

www.advmat.de

[54] H. Lee, H. Kim, I. Ha, J. Jung, P. Won, H. Cho, J. Yeo, S. Hong, S. Han, J. Kwon, K. J. Cho, S. H. Ko, *Soft Rob.* **2019**, *6*, 760.

[55] S. Song, S. Joshi, J. Paik, *Adv. Sci.* **2021**, *8*, 2100924.

[56] M. Sitti, *Extrem. Mech. Lett.* **2021**, *46*, 101340.

[57] Y. Yan, Y. Zhao, Y. Alsaid, B. Yao, Y. Zhang, S. Wu, X. He, *Adv. Intell. Syst.* **2021**, *3*, 2000234.

[58] H. Guo, M. O. Saed, E. M. Terentjev, *Adv. Mater. Technol.* **2021**, *6*, 2100681.

[59] M. D. Bartlett, N. Kazem, M. J. Powell-Palm, X. Huang, W. Sun, J. A. Malen, C. Majidi, *Proc. Natl. Acad. Sci. USA* **2017**, *114*, 2143.

[60] M. H. Malakooti, M. Zadan, N. Kazem, C. Majidi, *Proc. SPIE* **2021**, *11589*, 115890D.

[61] M. H. Malakooti, N. Kazem, J. Yan, C. Pan, E. J. Markvicka, K. Matyjaszewski, C. Majidi, *Adv. Funct. Mater.* **2019**, *29*, 1906098.

[62] Z. J. Patterson, A. P. Sabelhaus, K. Chin, T. Hellebrekers, C. Majidi, in *2020 IEEE/RSJ Int. Conf. on Intelligent Robots and Systems (IROS)*, IEEE, Piscataway, NJ, USA **2020**, pp. 8758–8764.

[63] J. Lee, H. Sul, Y. Jung, H. Kim, S. Han, J. Choi, J. Shin, D. Kim, J. Jung, S. Hong, S. H. Ko, *Adv. Funct. Mater.* **2020**, *30*, 2003328.

2200857 (11 of 11)

ADVANCED MATERIALS

Supporting Information

Liquid Crystal Elastomer with Integrated Soft Thermoelectrics for Shape Memory Actuation and Energy Harvesting

Mason Zadan, Dinesh K. Patel, Andrew P. Sabelhaus, Jiahe Liao, Anthony Wertz, Lining Yao, and Carmel Majidi*
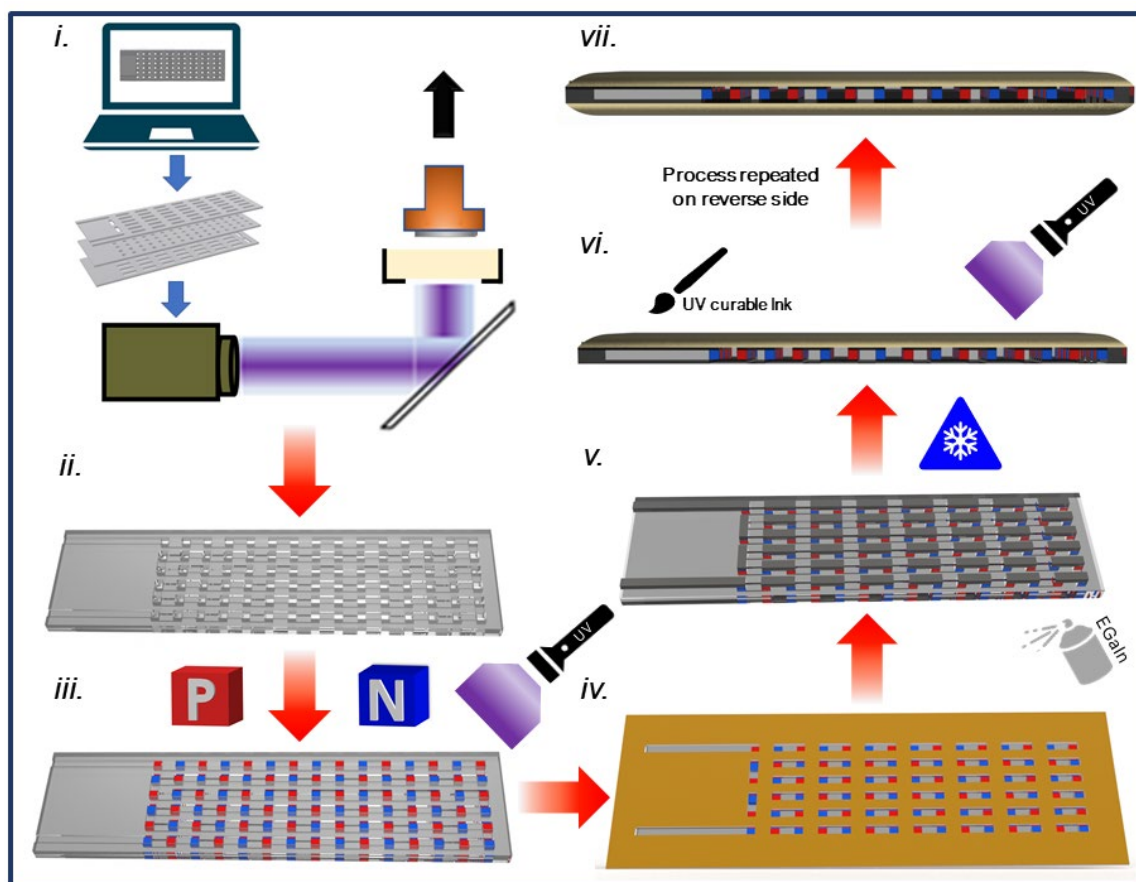
Supporting Information

Liquid Crystal Elastomer with Integrated Soft Thermoelectrics for Shape Memory Actuation and Energy Harvesting

Mason Zadan, Dinesh K. Patel, Andrew P. Sabelhaus, Jiahe Liao, Anthony Wertz, Lining Yao, Carmel Majidi[*]

Supplementary Figures

Figure S1. TED fabrication steps: i-ii) center layer and semiconductor substrate is printed using DLP printing process iii) P and N doped semiconductors are placed into the center layer and UV cured sealing them iv) A stencil is place overtop the center layer and EGaIn is airbrushed into the channels v) the stencil is removed and the device is placed in the freezer vi) a UV curable ink is brushed on in a thin layer and cured at 365nm for 12 mins vii) the process is repeated on the back side
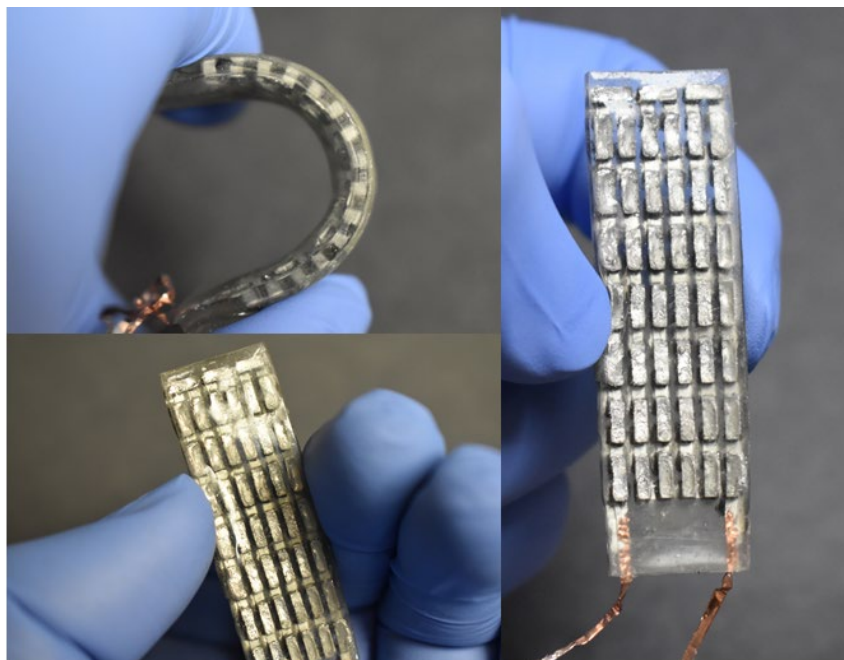
Figure S2. Images of completed 90 semiconductor TED before LCE has been adhered
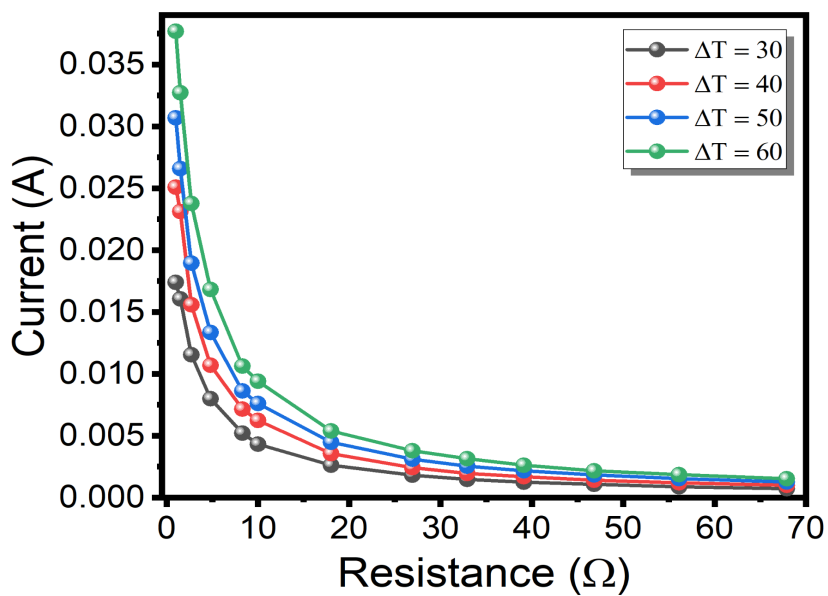
Figure S3. External resistance vs current for varying temperature differentials generated by a 90 semiconductor TED as seen in Figure S1. At a max temperature differential of 60 °C 38 mA was recorded at resistance of 1 Ω with current decreasing as resistance increased.
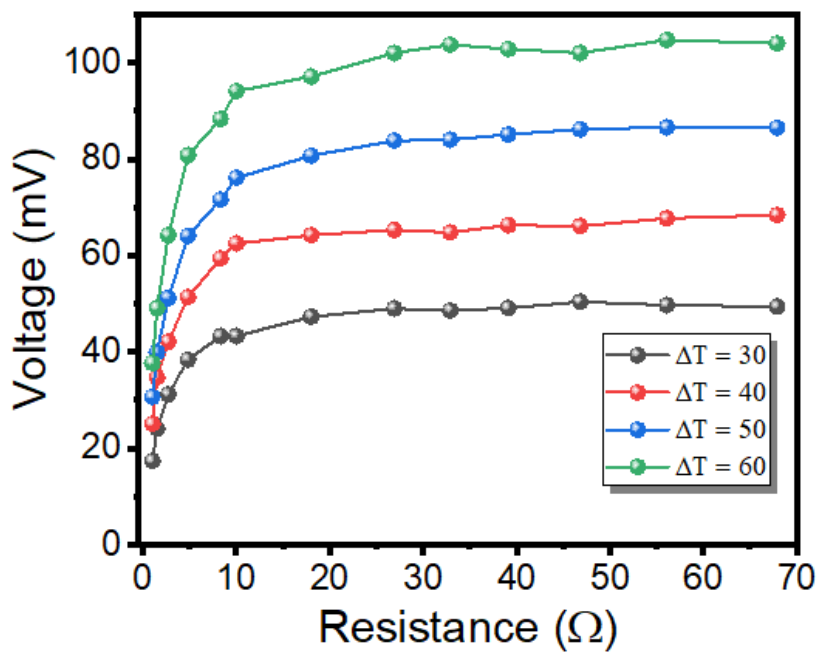
Figure S4. External resistance vs voltage for varying temperature differentials generated from a 90 semiconductor TED. An increase in resistance corresponds to a voltage that approaches the open circuit voltage above 10 Ω.
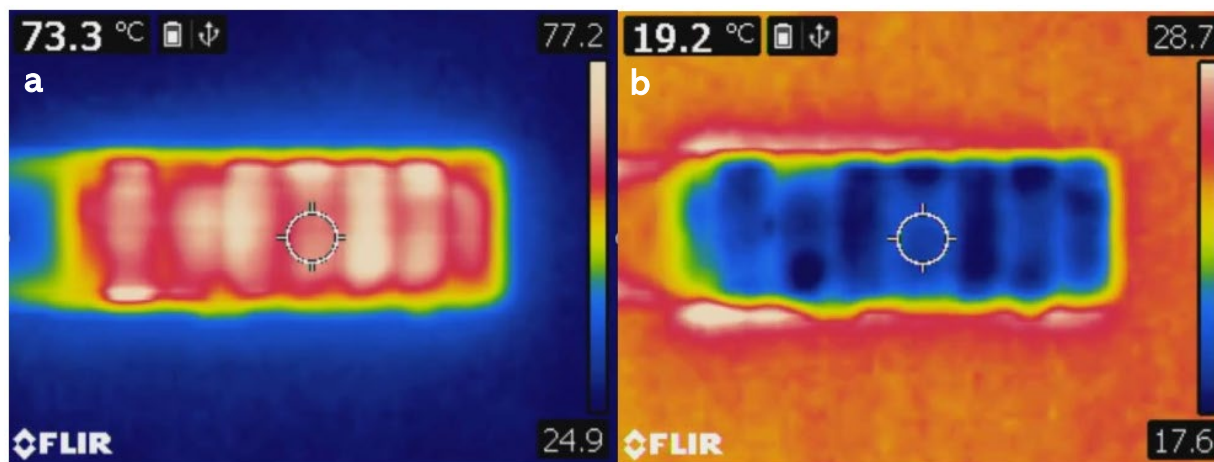
Figure S5. a) 90 semiconductor TED heating at 1.75A after 40s. b) 90 semiconductor TED cooling after 14s.
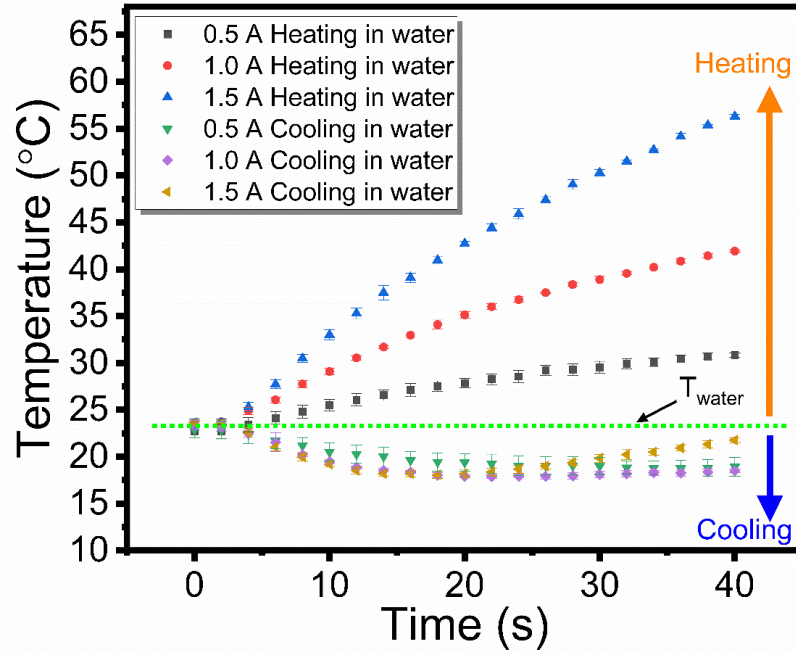
Figure S6. Comparison of Peltier heating and cooling for various currents. This test was conducted with the underside of the device in contact with water acting as a heat sink, and data recorded from the top side (n=3).
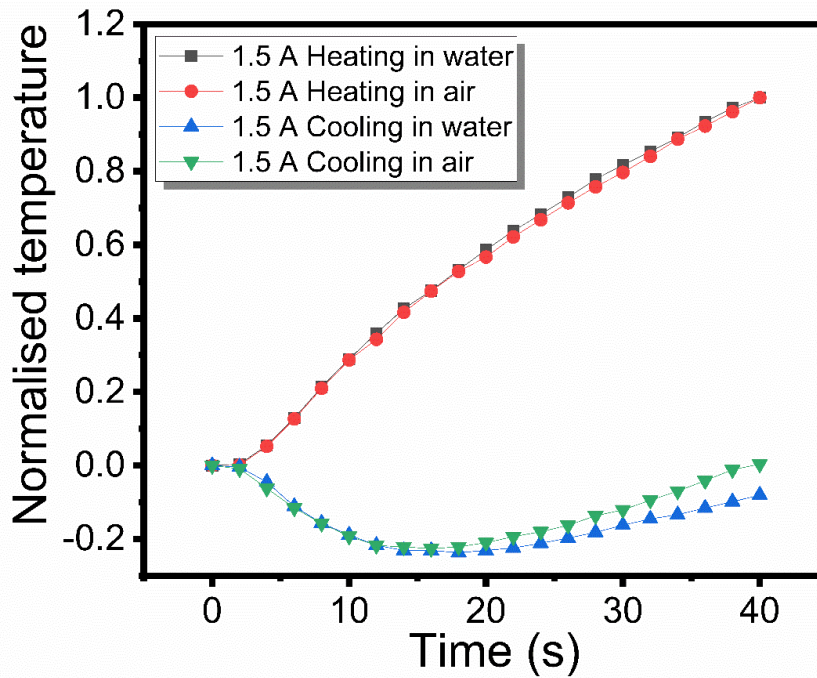
Figure S7. Comparison of Peltier heating and cooling data for ambient air conditions at 1.5 A (Figure 2c-d) and bottom side in water (Figure S6).

4

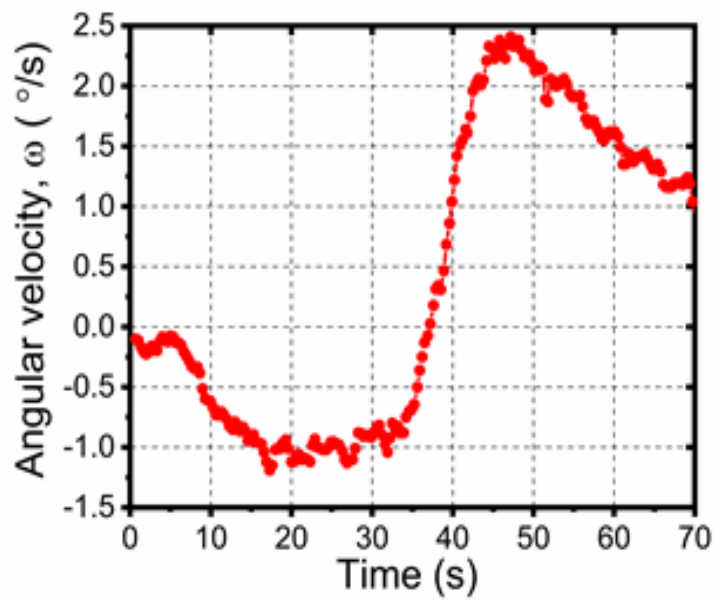Figure S8. Images of TEG-LCE Actuator

Figure S9. Angular velocity of 60 semiconductor actuator at 2.9V corresponding to Figure 3a.
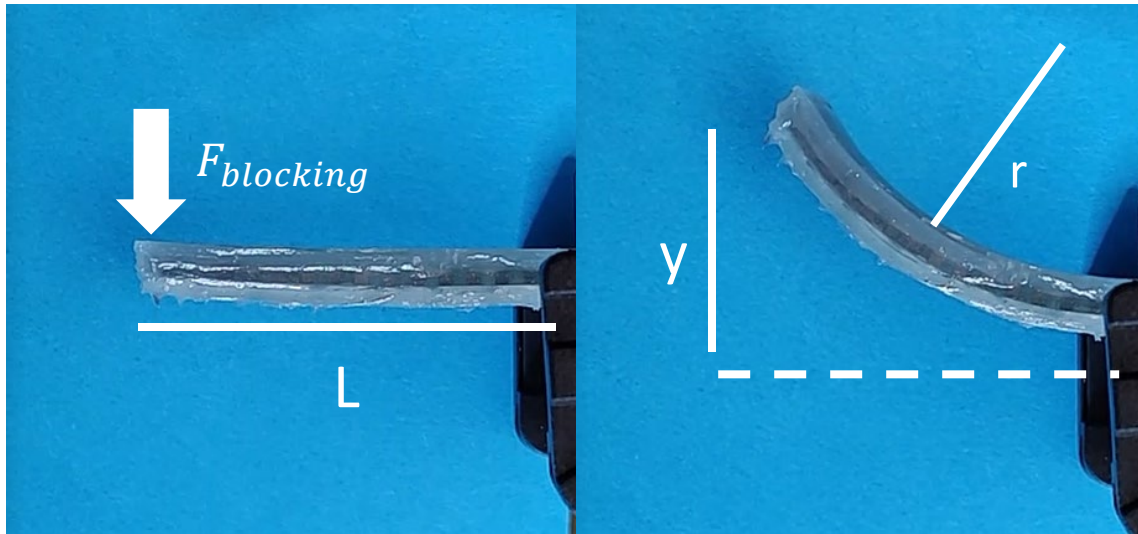
Figure S10. Diagram of actuator in initial vs actuated position with relevant dimensions for FoM calculations.
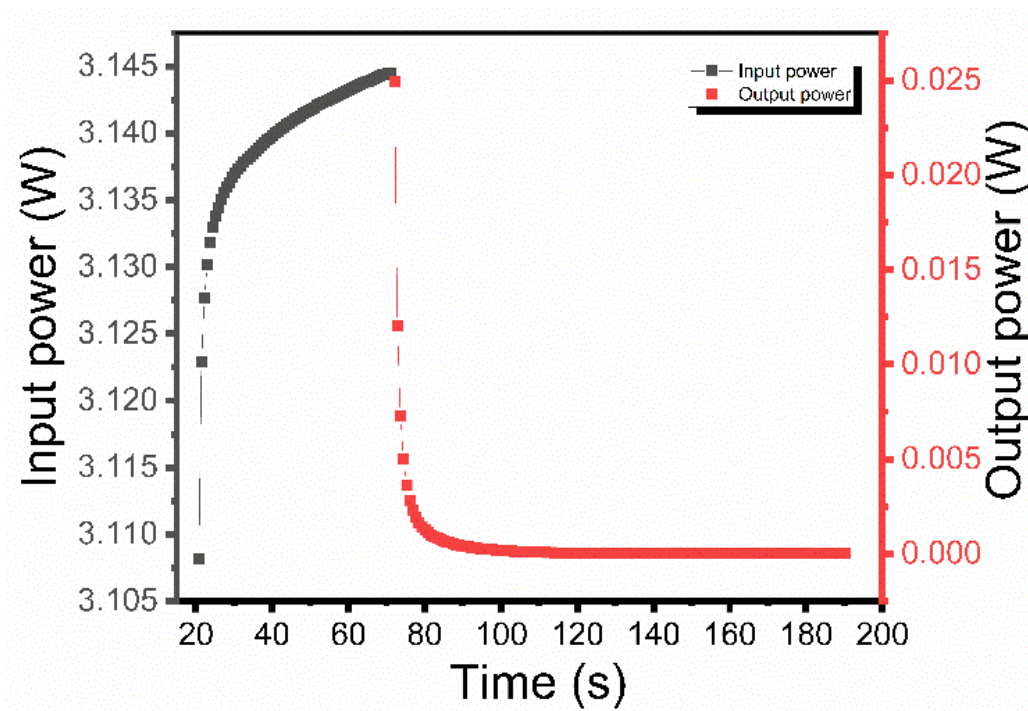

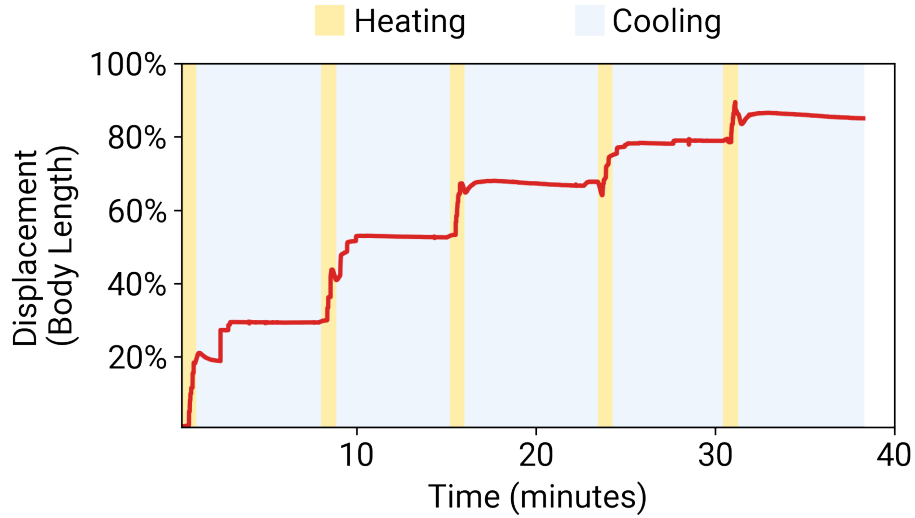Figure S11. Input and output power for the regenerative energy harvesting test for one cycle.

Figure S12. Graph of position vs time for 5 cycles of the soft robotics walker. Yellow heating sections are represented by the gait mechanics in Figure 4c. This is followed by a prolonged cool down time where the actuators passively regenerate energy. See Movie S1 for visual representation.
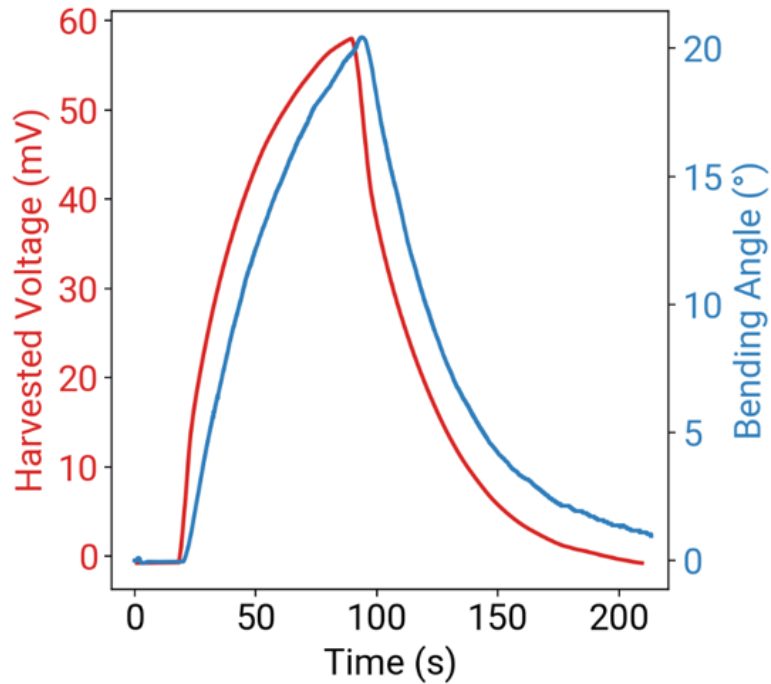

Figure S13. Bending angle and harvested voltage of LCE-TED bending towards a heat source exhibiting phototropism for increased harvested voltage. See Movie S3 and Figure 4f for corresponding figure.
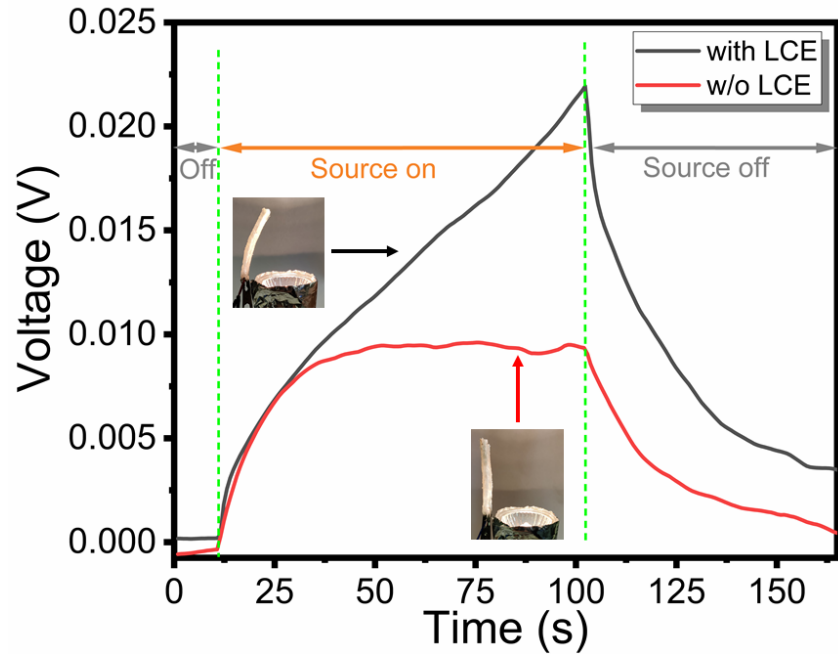
Figure S14. Results of phototropism inspired energy harvesting test. The transducer was placed above and parallel to a heat source with voltage collected with and without the LCE layer, highlighting the physical intelligence of this system track towards a heat source and increase voltage output.
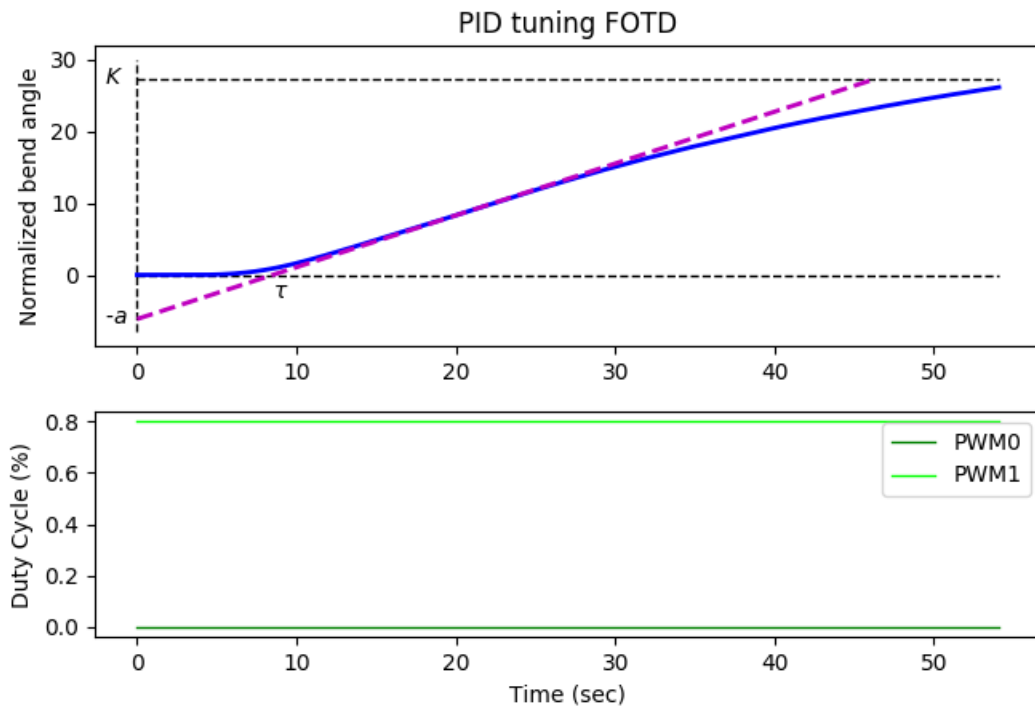
Figure S15. Step response test for tuning the proportional-integral (PI) controller for the LCE-TED soft limb. An 80% duty cycle PWM signal was applied to the forward-voltage gates of the H-bridge circuit for 55 sec., and the constants a, K, and τ were measured for use with the first-order plus time delay (FOTD) tuning methods.

Supplementary Materials and Methods

Table S1. 3D printing parameters for fabrication of soft and stretchable center layer

Printing parameters	Center layer
Slice Thickness (mm)	0.1
Exposure Time (s)	0.5
Burn-In Layers	1
Burn-In Exposure Time (s)	1.050
Light Intensity (mW/cm2)	27.84
Heater Temperature (°C)	40
Separation Velocity (mm/s)	1.000
Separation Distance (mm)	10.000
Approach Velocity (mm/s)	2.000
Slides Per Layer	1
Slide Velocity (mm/s)	10.000
Burn-In Wait Time (After Exposure)	5.000
Burn-In Wait Time (After Separation)	5.000
Burn-In Wait Time (After Approach)	5.000
Burn-In Wait Time (After Slide)	3.000
Normal Wait Time (After Exposure)	5.000
Normal Wait Time (After Separation)	5.000
Normal Wait Time (After Approach)	5.000
Normal Wait Time (After Slide)	5.000

Transducer Efficiency

Following the arguments in Lee et al.,[1] we define the figure of merit (FoM) of this transducer as:

$$\text{FoM} = \frac{U_e}{U_e + U_t} \tag{1.1}$$

where elastic energy and thermal energy is defined as

$$U_e = \frac{1}{2}Dk^2 \tag{1.2}$$

$$U_t = c_p m \Delta T \tag{1.3}$$

Here, D is the flexural rigidity, k is the bending curvature, $c_p = 1000$ J kg^{-1} K^{-1} [2,3] is the specific heat capacity for the heated LCE layer, $\Delta T = 43\ ^oC$ is the increase in temperature, and m = 8.4 × 10^{-4} kg is the LCE layer mass for one side.

We determine D and k from our empirical studies on actuator bending and blocking force. First, we note that for a cantilevered beam with an end load $F_{blocking}$, vertical displacement is described as

$$y = \frac{F_{blocking}L^3}{3D} \tag{1.4}$$

where L = 4.3×10^{-2} m is the length of beam and D is flexural rigidity. This relationship is based on Euler-Bernoulli beam theory, which relates a transverse point load and displacement for a beam that is initially straight. However, when the LCE-TED actuator is activated, it bends to form a circular arc. Nonetheless, based on the principle of linear superposition for a Euler-Bernoulli beam, we assume that Equ. (1.4) is a reasonable approximation even for a beam that is initially curved.

For an unloaded actuator that is able to freely bend, the maximum bending angle of 27 ° occurs at 35s when run at 2.9 V (Figure 3a). To estimate the corresponding displacement (y) we must first determine the curvature (k) of the bending actuator in the absence of a block force load. At 27 ° the radius formed by the arc length is r = 4.1×10^{-2} m. The curvature k is defined as

$$k = \frac{1}{r} = 24.4 \text{ m}^{-1} \tag{1.5}$$

and noting that the actuator bends into a circular arc, the vertical displacement that the blocking force load must overcome is calculated as

$$y = \frac{1-\cos kL}{k} = 0.021 \ m \qquad (1.6)$$

Referring to Figure 3e, an actuator that is constrained from bending will exert a blocking force of $F_{blocking} = 0.076$ N when activated at 2.9 V for 35s. Assuming that the actuator behaves like an Euler-Bernoulli beam, this implies that 0.076 N is approximately the force required to displace the tip of the beam by the amount y calculated in Equ. (1.6). Combining Equ. (1.4) and (1.6) implies that

$$\frac{F_{blocking}L^3}{3D} = \frac{1-\cos kL}{k}$$

Next, solving for D and inserting the values for $F_{blocking}$, L, and k yields

$$D = 1.6 \times 10^{-4} \ N \ m^2$$

Lastly, solving for U_e and U_t gives:

$$U_e = 4.80 \times 10^{-2} \ J$$

$$U_t = 36.12 \ J$$

This implies a figure of merit FoM = 0.0008.

Regenerative Energy Harvesting Efficiency

To estimate the energy efficiency of the LCE-TED transducer, a 60 semiconductor transducer, external power supply, external resistor, and multimeter (Agilent-34401a) were placed in the below circuit configuration (Circuit Diagram 1). This setup allows for continuous data collection in both the Peltier and Seebeck modes. The internal resistance of the device was $R_{TEG} = 2.3 \ \Omega$ with an external resistance of 2 Ω for impedance matching. The power source voltage was $V_{tot} = 3.2 \ V$ with V_{ext} being recorded by the multimeter during both Peltier and Seebeck modes (Figure S8). The power source was cycled on for 50s and off for 6 minutes. P_{input} and P_{output} were calculated:

$$P_{input} = V_{tot}V_{ext}\left[\frac{1}{R_{TEG}} + \frac{1}{R_{ext}}\right] - \frac{V_{ext}^2}{R_{ext}} \tag{2.1}$$

$$P_{output} = \frac{V_{ext}^2}{R_{ext}} \tag{2.2}$$

which were obtained from the relationship

$$P = VI = I^2R = \frac{V^2}{R} \tag{2.3}$$
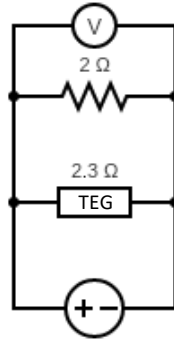
Energy was then calculated by numerical integrating power over input and output cycle times with energy efficiency calculated as η:

$$E_{input} = \int P_{input}dt \tag{2.4}$$

$$E_{output} = \int P_{output}dt \tag{2.5}$$

$$\eta = \frac{E_{output}}{E_{input}} \times 100 \tag{2.6}$$

Circuit Diagram 1

Feedback Control Design

Our proportional-integral (PI) feedback controller was tuned using well-known methods from the literature. Thanks to our ability to apply a control input that cools the device - a *negative voltage* - these tuning rules are now applicable. With heating alone, a PI controller would attempt to apply a negative control input and would incorrectly saturate at 0V.

Tuning of a PI controller can be performed in a number of ways. We chose to use the time domain step response method,[4] where a constant control input was applied and various properties

of the resulting trajectory are used to estimate the proportional (K_p) and integral (K_i) constants. We chose an 80% duty cycle input step, representative of the actuator during its aggressive operation, mapped to the PWM that controlled the "forward" signal of the H-bridge circuit.

Figure S15 shows the step response alongside the three tuning constants that are used in the first-order plus time delay method. Note that the approximated time delay, τ, is very large (approx. 8.5 sec), making high-performance control challenging without an accurate system model. Since our actuator can overheat after application of significant power over a long period of time, we chose not to perform a step response test where the system fully settled to a steady-state value.

We used three methods[4] to estimate feedback gains from these step response parameters. These included the Zeigler-Nichols method and its two modifications to include the settling value of the step response, K (Figure S15). Averaging the estimated gains gave $K_p = 0.096, K_i = 4 \times 10^{(-2)}$. It is well known that these gains, when applied to a nonlinear system, provide only an initial guess. Executing our controller with these gains showed significant oscillations, primarily due to the time delay. After adjustments by hand, our final controller used $K_p = 0.08, K_i = 2 \times 10^{(-6)}$, representing significantly lower integral control.

Finally, note that although our PI controller could potentially saturate above 100% or below -100% duty cycle, we did not observe such behavior (Figure 4b, main text). As a result, integral windup was not observed and no compensation is needed, though there would be simple techniques to do so if required.[5] Similarly, our controller did not perform the most aggressive actions possible for fast operation: control inputs never reached maximum power, and so the actuator necessarily responded slower than could have otherwise been possible. Many improvements can be made for better performance, including sliding mode control or other model-based methods. However, our simple controller validates the concept while highlighting the benefits of active cooling.

References

[1]   H. Lee, H. Kim, I. Ha, J. Jung, P. Won, H. Cho, J. Yeo, S. Hong, S. Han, J. Kwon, K. J. Cho, S. H. Ko, *Soft Robot.* **2019**, *6*, 760.

[2]   A. Kotikian, J. M. Morales, A. Lu, J. Mueller, Z. S. Davidson, J. W. Boley, J. A. Lewis, *Adv. Mater.* **2021**, *33*, 1.

[3]   M. J. Ford, C. P. Ambulo, T. A. Kent, E. J. Markvicka, C. Pan, J. Malen, T. H. Ware, C. Majidi, *Proc. Natl. Acad. Sci. U. S. A.* **2019**, *116*, 21438.

[4]   K. J. Astrom, T. Hagglund, *Advanced PID Control*, ISA-The Instrumentation Systems And Automation Society, Research Triangle Park NC, **2006**.

[5]   K. J. Aström, R. M. Murray, *Feed. Syst.* **2008**, 408.